Characterization of He Induced Nanostructures Using SEM Image Analysis*)

Hirohiko TANAKA, Shin KAJITA[1] and Noriyasu OHNO

Graduate School of Engineering, Nagoya University, Chikusa-ku, Nagoya 464-8603, Japan
[1]*Institute of Materials and Systems for Sustainability, Nagoya University, Chikusa-ku, Nagoya 464-8603, Japan*

Helium induced nanostructures on tungsten were characterized by applying basic statistical analysis techniques to scanning electron microscope (SEM) images. As the analysis targets, pinhole- and fuzz-dominant surfaces irradiated with different ion fluences were employed. Although two-dimensional Fourier analysis of the normalized brightness of SEM images clarified several characteristic features, their differences are small to distinguish the dominant nanostructures. On the other hand, probability density functions (PDFs) of the normalized brightness indicate that hole- and fuzz-dominant surfaces have long tail and Gaussian-like shape, respectively. By using several indexes with considering the black and white saturation, it was found that kurtosis and Kullback-Leibler divergence could provide reasonable judgement as the characterization index.

1. Introduction

Tungsten (W) is thought to be the most promising material for the divertor target that should be irradiated with the high heat and particle fluxes in future magnetic fusion devices. From past researches, although W has quite low sputtering rate, helium (He) plasma irradiation could provoke several kinds of surface modifications such as bubbles, pinholes, and fiberform nanostructures called *fuzz*, even if the incident ion energy was much smaller than the sputtering threshold [1]. Up to now, the fuzz-formation condition was deeply investigated and was found to be strongly related to the incident ion energy, surface temperature, and ion fluence [2]. Fuzzy nanostructure changes several surface physical characteristics, e.g., high light absorptivity [3] and large surface area [4] due to an increase of the porosity [5]. Further, similar nanostructures are also found to be formed on other metals such as iron [6], vanadium [7], platinum, and so on [8–10]. In order to utilize the unique characteristics of the fuzzy surface for an industrial application field, morphology-change conditions of several metals are energetically being surveyed.

The novel growth process of fuzzy structure has been attracted attention from modeling perspective. Density functional theory (DFT) and molecular dynamics (MD) were used for the nucleation of He clusters and bubbles and dislocation formation [11–14], and morphology changes were demonstrated using multi-scale simulations by the combination of MD and Monte Carlo (MC) simulations [15, 16]. Even though those simulations still have a challenging issue that they can only deal with a limited time and space, formations of initial protrusion and short fine structures were demonstrated.

To bridge the experiments and simulation, it is necessary to compare the grown structure quantitatively; fractal analysis has been conducted using scanning electron microscope (SEM) micrographs, transmission electron microscope (TEM) micrographs, and gas adsorption isotherms [17–19]. It was found that initially formed pinholes have a fractal feature in the size-number relation and the fuzzy structure has a multi-fractal feature. It is of interests to further develop method to extract the specific characteristics of fuzzy structures grown by He plasma irradiation.

In this study, we applied basic statistical analysis techniques based on two-dimensional (2D) fast Fourier transform (FFT) and probability density function (PDF) to SEM images. As the He ion fluence increases, the fuzzy surface was formed with accompanying changes of several statistical features. By introducing characterizing statistics and a measuring scale of PDFs, pinhole- and fuzz-dominant images were distinguished. Such techniques are easy to apply. Thus, these techniques could be easily shared among researchers and would be utilized for the parameter survey from a number of samples.

In Sec. 2, analyzed SEM images will be explained. Then, these images will be analyzed in Sec. 3. Finally, this study will be summarized in Sec. 4.

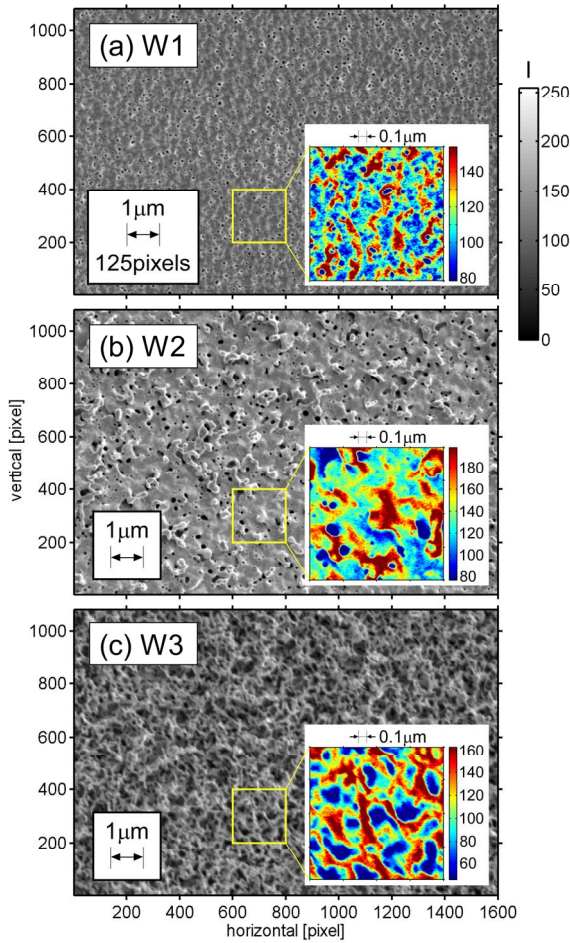*author's e-mail: h-tanaka@ees.nagoya-u.ac.jp*

Fig. 1   Analyzed SEM images of W samples: (a) W1, (b) W2, and (c) W3. Insets show magnified figures with the color scale from $\mu - 1.5\sigma$ to $\mu + 1.5\sigma$.

Fig. 2   2D power spectra of I_n of (a) W1, (b) W2, and (c) W3 along k_h and k_v.

2. Analyzed SEM Images

We analyzed three W samples irradiated with He plasmas at different fluences in the linear plasma device NAGDIS-II [19]. Figure 1 shows the analyzed SEM images: W1, W2, and W3, which are viewed from the normal direction to the surface. The He ion fluences of W1, W2, and W3 are 6×10^{24}, 1.8×10^{25}, and 4.7×10^{25} m^{-2}, respectively. Sample information and irradiation conditions are summarized in Table 1 of Ref. [19]. On W1 surface, a number of pinholes can be found. As increasing the fluence, thicker convex structures appear in addition to pinholes (see Fig. 1 (b)), and then, fuzzy nanostructure covers the surface (see Fig. 1 (c)).

Brightness (I) of these images is 8-bit grayscale which has 256 tonal steps from $I = 0$ (black) to 255 (white). The analyzed size of each image is 1080 pixels in vertical direction and 1600 pixels in horizontal direction.

3. Image Analyses

As the basic technique for the image analysis, 2D FFT and PDF analyses were applied. For analyzing SEM images, it should be taken into account that the mean of the
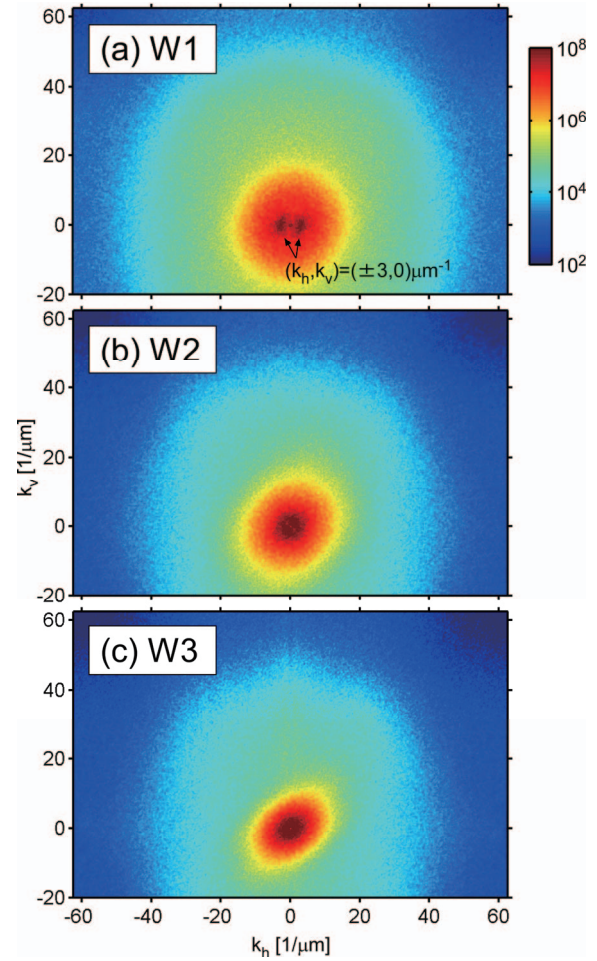
brightness and the contrast can be changed depending on SEM devices, and beam and detector settings. Furthermore, saturations in the brightness can occur depending on the settings.

In this study, to minimize the effects, the normalized brightness, $I_n \equiv (I - \mu)/\sigma$, was used for the analyses, where μ and σ are the mean and the standard deviation of I in all pixels, respectively. Effects from the black and white saturation for 2D FFT and PDF analyses will be discussed later. Insets in Fig. 1 are magnified images with the color scale from $\mu - 1.5\sigma$ to $\mu + 1.5\sigma$. Their characteristic features associated with the analyses will be discussed in Sec. 3.1.

3.1   2D FFT

2D FFT analysis is widely used for identifying the crystalline nature particularly on TEM images [20, 21]. We investigated whether the 2D FFT analysis could find a dominant nanostructure from SEM images.

Figures 2 (a, b, c) shows 2D power spectra of I_n of W1, W2, and W3. Before the application of the 2D FFT, Hanning window was applied to minimize the edge effect. Horizontal and vertical axes indicate the wave numbers, k_h and k_v, along horizontal and vertical axes in Fig. 1,

respectively. Because a 2D power spectrum has a point symmetric profile, $k_v < -20\,\mu\mathrm{m}^{-1}$ range is not displayed in Figs. 2 (a, b, c).

At around $(k_h, k_v) \sim (\pm 3, 0)\,\mu\mathrm{m}^{-1}$ in Fig. 2 (a), there are unemphatic small peaks, indicating that there is a vertical-stripe component with a characteristic length of $\sim 1/3\,\mu\mathrm{m}$. Actually, in the inset in Fig. 1 (a), concavo-convex structures seem to be elongated not in the horizontal direction but in the vertical direction. This would reflect a stripe formation on single crystal W surfaces in the initial phase of He plasma irradiation [22]. In addition, profile of the 2D power spectrum of W3 seems to be slightly elongated to the $k_h k_v > 0$ direction, implying that characteristic length in the right oblique direction is slightly shorter than that in the left oblique direction. However, in any case, the spectral shape roughly looks like a concentric pattern.

Figure 3 (a) is azimuthally averaged power spectra of Figs. 2 (a, b, c) along $k = (k_h^2 + k_v^2)^{1/2}$. A little convex of W1 at $k \sim 3\,\mu\mathrm{m}^{-1}$ is attributed to the above-mentioned vertical-stripe structures. A shoulder of W1 exists at $k \sim 10\,\mu\mathrm{m}^{-1} = (0.1\,\mu\mathrm{m})^{-1}$, and the wave number corresponds to the inverse of the typical diameter of pinholes ($\sim 0.1\,\mu\mathrm{m}$) shown in the inset in Fig. 1 (a). Such shoulder is observed when similar-size structures are nonperiodically distributed [23]. Thus, it is found that pinholes are distributed nonperiodically. The power spectra of W3 has large component at smaller k range, indicating that the fuzz forms a larger-scale rough surface compared with the typical size of pinholes on W1. Actually, submicrometer structures can be found in the inset in Fig. 1 (c). These larger-scale structures have no periodicity, because there is no spectral peak. The power spectrum of W2 looks like an intermediate between power spectra of W1 and W2. This

would be caused by the coexistence of pinholes and initial structures of fuzz.

In order to investigate the effect from the black and white saturation for these power spectra, artificially saturated images were analyzed. In this calculation, pixels with I less than $\mu - 1.5\sigma$ and over than $\mu + 1.5\sigma$ were replaced with -1.5σ and 1.5σ values, respectively. These artificially saturated images, which correspond to the insets in Fig. 1, were normalized again and then analyzed with the 2D FFT. Figure 3 (b) shows the power spectra of the artificially saturated images. There is no clear difference between Fig. 3 (a) and Fig. 3 (b), indicating that a certain level of the black and white saturation is not a problem for the 2D FFT analysis.

From the analysis results, we found several characteristic features in three samples. However, because pinholes and fuzz have no periodicity, it is not easy to distinguish these structures from 2D FFT analysis.

3.2 PDF

Next, we applied the PDF analysis. Figure 4 shows histograms of brightness I of three samples. They have peaks near the middle of the 256 tonal steps. Histograms of W1 and W3 become quite small at both ends. On the other hand, the histogram of W2 has small peaks at $I = 0$ and 255, being attributable to the black and white saturation. Because the edge peaks largely affect the below-mentioned PDF analysis result in contrast to the power spectra, both ends of all histograms ($\sim 2\%$ in each end) were removed before the following analysis.

Figure 5 is semilogarithmic plots of PDFs as a function of I_n. Integration of each PDF is equal to unity. PDF tails are located within the range of $-5 \le I_n \le 5$ except for a tail with a small amplitude in positive I_n region of W1. In each figure, the standard Gaussian distribution ($\mu = 0$ and $\sigma = 1$) is overplotted as a reference.

We can find significant differences between Figs. 5 (a, b) and Fig. 5 (c). The PDFs of W1 and W2 have tails in the negative I_n region with large amplitudes due to the existence of pinholes, which have darker colors ($I_n < 0$). The
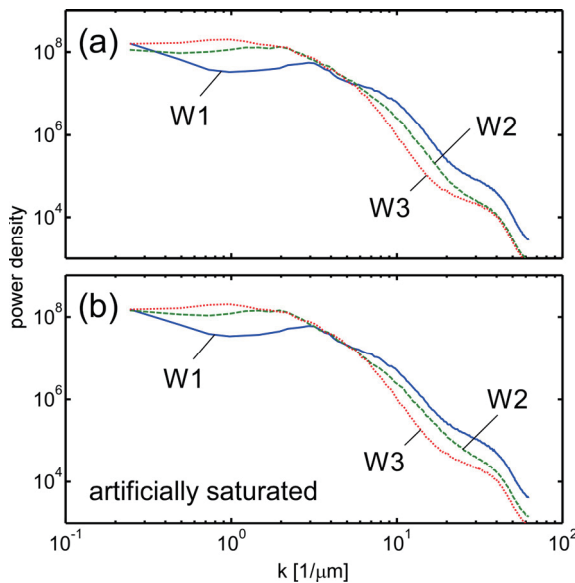

Fig. 3 Azimuthally averaged power spectra of (a) I_n and (b) artificially saturated and then normalized I_n of W1 (solid), W2 (dashed), and W3 (dotted) along k.
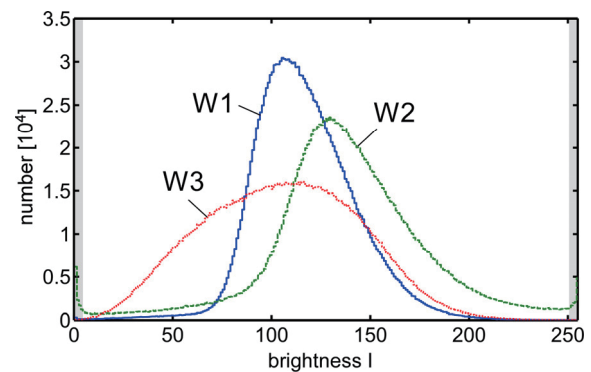

Fig. 4 Histograms of brightness of W1 (solid), W2 (dashed), and W3 (dotted).
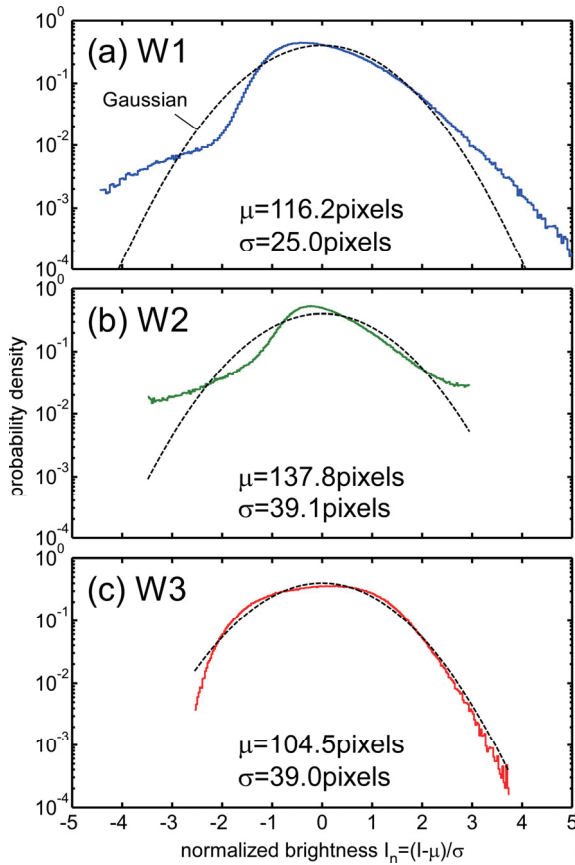
Fig. 5   PDFs of (a) W1, (b) W2, and (c) W3 as a function of the normalized brightness. Black dashed lines indicate the standard Gaussian distribution.

PDFs of W1 and W2 in the positive I_n region have also larger amplitudes compared with the Gaussian distribution. This is mainly caused by brighter regions from the edge of pinholes and convex structures, because SEM image has higher brightness at the edge of structures due to secondary electron emissions from the edge face. In contrast, the PDF of W3 has no long tail and resembles the Gaussian shape due to the complicated fuzzy nanostructures. From Fig. 5, it is suggested that pinholes and fuzz could be distinguished by comparing the PDF with the Gaussian distribution.

For characterizing a PDF, skewness (S) and kurtosis (K) are convenient indexes and often used in edge plasma field [24]. They are defined by

$$S \equiv \frac{\left\langle (I-\mu)^3 \right\rangle}{\sigma^3} = \left\langle I_n^3 \right\rangle, \tag{1}$$

$$K \equiv \frac{\left\langle (I-\mu)^4 \right\rangle}{\sigma^4} - 3 = \left\langle I_n^4 \right\rangle - 3, \tag{2}$$

where $\langle \ \rangle$ means an average. Since the Gaussian distribution has $S = K = 0$, S and K values are utilizable for comparison with the Gaussian. If a PDF had a large amplitude at positive/negative I_n tail region, S became positive/negative. Thus, the sign is important for S. On the
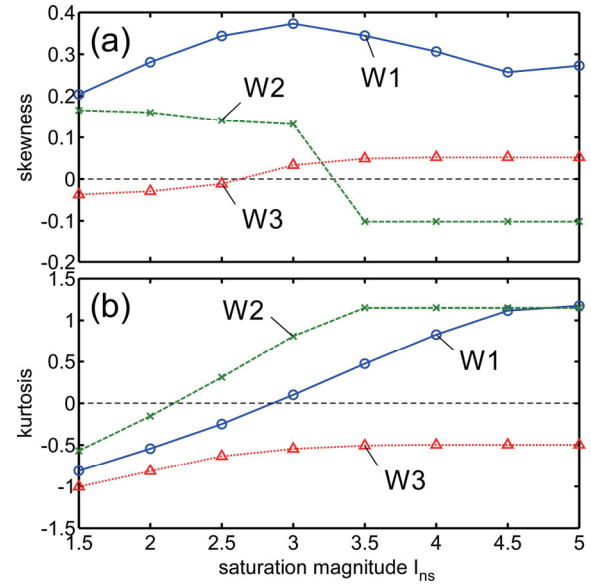

Fig. 6   (a) Skewness and (b) kurtosis of W1 (solid), W2 (dashed), and W3 (dotted) as a function of I_{ns}.

other hand, positive and/or negative longer tail compared with the Gaussian produces $K > 0$. Shorter tails in positive and negative directions make K negative.

Because the tail components are important for S and K calculations, the effect from the black and white saturation should be taken into account. In order to confirm whether these statistics could be utilized quasi-universally for SEM images, sensitivities of S and K against the saturation were investigated by artificially limiting the I_n range. In the following, signals satisfying $|I_n| > I_{ns}$ were removed and a normalized brightness was then recomputed before the S and K estimations by introducing a saturation magnitude I_{ns}.

Figure 6 shows the skewness and kurtosis as a function of I_{ns}. At $I_{ns} = 5$, where almost all data was used, S of W1 is the largest in the three samples (see Fig. 6 (a)). As changing I_{ns}, S of W1 maintains the largest, while sign of S switches on W2 and W3 samples. Considering the sensitivities of S-sign on I_{ns}, discrimination of surface nanostructures seems to be difficult from S. On the other hand, K of W1 and W2 are larger than that of W3 for all I_{ns} cases. Furthermore, except for small I_{ns} cases, K of W1 and W2 are positive and that of W3 is negative. This is caused by existence/nonexistence of the PDF tail. Therefore, K is a possible candidate for the characterization index.

As a different candidate, Kullback-Leibler divergence (KLD) [25] is considered to compare the PDF with the Gaussian. The KLD is a famous scale for measuring difference between two PDFs in probability and information theory fields and is also called "information divergence" and "relative entropy". In plasma field, KLD was applied to turbulent signals [26]. The KLD (D_{KL}) of a PDF (P) against a different PDF (Q) distributing on the I_n axis is defined as follows:
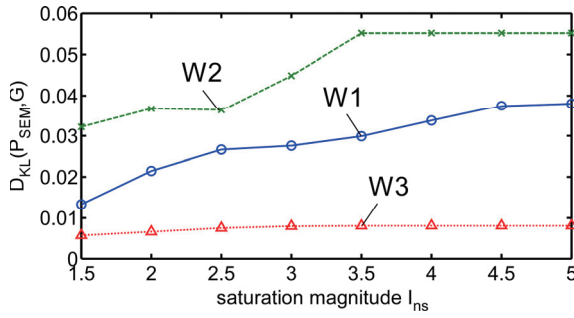
Fig. 7 $D_{KL}(P_{SEM}, G)$ of W1 (solid), W2 (dashed), and W3 (dotted) as a function of I_{ns}.

$$D_{KL}(P, Q) \equiv \int_{-\infty}^{\infty} P(I_n) \log\left(\frac{P(I_n)}{Q(I_n)}\right) dI_n. \tag{3}$$

The D_{KL} value is nonnegative, and D_{KL} becomes zero when P and Q are the same. Although the KLD is also called "KL distance", this is not a distance function, because $D_{KL}(P, Q) \neq D_{KL}(Q, P)$.

In order to compare between a PDF from a SEM image (P_{SEM}) and the Gaussian (G), $D_{KL}(P_{SEM}, G)$ and $D_{KL}(G, P_{SEM})$ can be calculated. Ideally, integration range in Eq. (3) is from $-\infty$ to ∞. However, far-edge tails are not acquired in a PDF from a SEM image due to the limited tonal range. Because $P \log(P/Q) = 0$ and ∞ when $P = 0$ and $Q = 0$, respectively, $D_{KL}(P_{SEM}, G)$ has a finite value and $D_{KL}(G, P_{SEM})$ becomes infinity if the integration range contains a $P_{SEM} = 0$ region. Therefore, $D_{KL}(P_{SEM}, G)$ was only calculated as a function of I_{ns}, as shown in Fig. 7. Before the D_{KL} calculation, signals satisfying $|I_n| > I_{ns}$ were removed, and then the integral of the P_{SEM} was calibrated to be unity. In all I_{ns} range, $D_{KL}(P_{SEM}, G)$ of W3 is much smaller than those of W1 and W2. Thus, $D_{KL}(P_{SEM}, G)$ could be used for distinguish SEM images.

4. Summary

In order to characterize He induced nanostructures, we applied two basic analysis techniques to SEM images: 2D power spectrum and probability density function. To minimize the effects from the differences in contrast and brightness levels of SEM images, the normalized brightness was analyzed with taking into account of the black and white saturation.

From the 2D power spectra, nondirectional and non-periodic features of pinholes and fuzz are found. Because differences of these spectra are not significant, this method would be inadequate for distinguishing pinhole- and fuzz-dominant structures with the non-periodic nature.

In contrast, probability-density-function shapes calculated from the brightness have a significant difference between pinhole- and fuzz-dominant surfaces. The former surface has long tails in the PDF, while latter surface has a Gaussian-like shape. As a result, positive and negative kurtosis are observed in pinhole- and fuzz-dominant images, respectively, as if a certain level of brightness is saturated. Further, Kullback-Leibler divergence clearly indicates a resemblance with the Gaussian. In order to distinguish pinhole- and fuzz-dominant SEM images, the kurtosis and the Kullback-Leibler divergence would be useful.

For future work, it is of interests to apply the above-mentioned techniques to a number of SEM images with various nanostructures. Application of such characterization indexes would make it easy for researchers to survey parameter dependences. Further, above techniques could be applied to surfaces made in a computer simulation.

[1] S. Takamura, N. Ohno, D. Nishijima and S. Kajita, Plasma Fusion Res. **1**, 051 (2006).
[2] S. Kajita, W. Sakaguchi, N. Ohno, N. Yoshida and T. Saeki, Nucl. Fusion **49**, 095005 (2009).
[3] S. Kajita, T. Saeki, N. Yoshida, N. Ohno and A. Iwamae, Appl. Phys. Express **3**, 085204 (2010).
[4] M. Yajima, Y. Hatano, S. Kajita, J. Shi, M. Hara and N. Ohno, J. Nucl. Mater. **438**, S1142 (2013).
[5] D. Nishijima, M. Baldwin, R. Doerner and J. Yu, J. Nucl. Mater. **415**, S96 (2011).
[6] S. Kajita, T. Yoshida, D. Kitaoka, R. Etoh, M. Yajima, N. Ohno, H. Yoshida, N. Yoshida and Y. Terao, J. Appl. Phys. **113**, 134301 (2013).
[7] S. Kajita, T. Yoshida, N. Ohno, Y. Ichino and N. Yoshida, J. Phys. D: Appl. Phys. **51**, 215201 (2018).
[8] S. Kajita, T. Nojima, Y. Tomita, N. Ohno, H. Tanaka, N. Yoshida, M. Yajima, T. Akiyama, M. Tokitani and T. Yagi, Surf. Coat. Technol. **340**, 86 (2018).
[9] S. Takamura and Y. Uesugi, Appl. Surf. Sci. **356**, 888 (2015).
[10] Y. Ueda, N. Yamashita, K. Omori, H.L. Lee, K. Ibano and A.M. Ito, J. Nucl. Mater. **511**, 605 (2018).
[11] C.S. Becquart and C. Domain, Phys. Rev. Lett. **97**, 196402 (2006).
[12] T. Tamura, R. Kobayashi, S. Ogata and A.M. Ito, Model. Simul. Mater. Sci. Eng. **22**, 015002 (2014).
[13] A.M. Ito, Y. Yoshimoto, S. Saito, A. Takayama and H. Nakamura, Phys. Scr. **T159**, 014062 (2014).
[14] R. Kobayashi, T. Hattori, T. Tamura and S. Ogata, J. Nucl. Mater. **463**, 1071 (2015).
[15] A. Lasa, S.K. Tähtinen and K. Nordlund, Europhys. Lett. **105**, 25002 (2014).
[16] A.M. Ito, A. Takayama, Y. Oda, T. Tamura, R. Kobayashi, T. Hattori, S. Ogata, N. Ohno, S. Kajita, M. Yajima, Y. Noiri, Y. Yoshimoto, S. Saito, S. Takamura, T. Murashima, M. Miyamoto and H. Nakamura, Nucl. Fusion **55**, 073013 (2015).
[17] S. Kajita, Y. Tsuji and N. Ohno, Phys. Lett. A **378**, 2533 (2014).
[18] S. Kajita, N. Yoshida, N. Ohno and Y. Tsuji, New J. Phys. **17**, 043038 (2015).
[19] S. Kajita, A.M. Ito and N. Ohno, Phys. Lett. A **381**, 2355

(2017).

[20] N. Yoshizawa, Y. Yamada and M. Shiraishi, J. Mater. Sci. **33**, 199 (1998).

[21] J.H. Warner, M.H. Rümmeli, A. Bachmatiuk, M. Wilson and B. Büchner, ACS Nano **4**, 470 (2010).

[22] N. Ohno, Y. Hirahata, M. Yamagiwa, S. Kajita, M. Takagi, N. Yoshida, R. Yoshihara, T. Tokunaga and M. Tokitani, J. Nucl. Mater. **438**, S879 (2013).

[23] H. Tanaka, N. Ohno, N. Asakura, Y. Tsuji, H. Kawashima, S. Takamura, Y. Uesugi and the JT-60U Team, Nucl. Fusion **49**, 065017 (2009).

[24] O.E. Garcia, J. Horacek, R.A. Pitts, A.H. Nielsen, W. Fundamenski, V. Naulin and J.J. Rasmussen, Nucl. Fusion **47**, 667 (2007).

[25] S. Kullback, *Information Theory and Statistics* (John Wiley and Sons, Inc., New York, 1959) pp. 825-827.

[26] V. Budaev, Y. Kikuchi, Y. Uesugi and S. Takamura, Nucl. Fusion **44**, S108 (2004).